Targeting p16^{INK4a} reverses alveolar epithelial cell dysfunction and induces lung regeneration in emphysema

Bruno Ribeiro Baptista (1, 2, 3)*, Marylène Toigo (1)*, Grégoire Justeau (1), Perla Abou-Atmeh (1), Thalles de Freitas Castro (1), Maéva Zysman (1, 4), Charlotte Thiebaut De Menonville (1), Etienne Audureau (1, 5), Klara Schnyder (6, 8), Huijuan Wang (6, 7, 8), Yan Hu (9), Melanie Königshoff (9), Sophie Lanone (1), François Chabot (2, 3), Elodie Zana-Taïeb (1), Claude Jourdan Le Saux (10), Mareike Lehmann (12, 13, 14), Geneviève Derumeaux (1, 15), Jorge Boczkowski (1), Janine Gote-Schniering (6, 8, 11)#*, Laurent Boyer (1, 15)#*

1. Université Paris Est Créteil (UPEC), FHU SENCODE, IMRB, INSERM, Créteil, France
2. Département de Pneumologie, CHRU NANCY, Vandœuvre-lès-Nancy, France
3. Université de Lorraine, INSERM, UMR_S 1116, DCAC, Vandœuvre-lès-Nancy, France
4. Centre de Recherche cardio-thoracique de Bordeaux, U1045, Université de Bordeaux, Pulmonary Department, Centre Hospitalier Universitaire (CHU), Bordeaux, France
5. Department of Public Health, Hôpitaux Universitaires Henri Mondor, AP-HP, Créteil, France
6. Department of Rheumatology and Immunology, Inselspital, Bern University Hospital, University of Bern, Switzerland
7. Graduate School for Cellular and Biomedical Sciences, University of Bern, Switzerland
8. Lung Precision Medicine (LPM), Department for BioMedical Research (DBMR), University of Bern, Bern, Switzerland
9. Division of Pulmonary, Allergy, Critical Care, and Sleep Medicine, Department of Medicine University of Pittsburgh, Pittsburgh, PA, USA.
10. Department of Medicine, Division of Pulmonary, Critical Care, Allergy, and Sleep Medicine, University of California San Francisco, San Francisco, California, USA.
11. Department of Pulmonary Medicine, Allergology and Clinical Immunology, Inselspital, Bern University Hospital, University of Bern, Switzerland
12. Institute for Lung Research, Philipps-University Marburg, Member of the German Center for Lung Research (DZL), Marburg, Germany.
13. Comprehensive Pneumology Center (CPC), Institute of Lung Health and Immunity, Helmholtz Zentrum München, Member of the German Center for Lung Research (DZL), Munich, Germany

14. Institute for lung health (ILH), Giessen, Germany.
15. Département de Physiologie-Explorations Fonctionnelles, Hôpitaux Universitaires Henri Mondor, AP-HP, Créteil, France

* These two authors participated equally to this work.

shared correspondence

Keywords: regeneration, $p16^{INK4a}$, epithelial cells, emphysema

Abstract

Pulmonary emphysema involves impaired regenerative capacity of alveolar type 2 epithelial cells (AT2), the main progenitor cells in alveoli. However, the mechanisms underlying dysfunctional epithelial repair remain unclear. In a mouse model of elastase-induced emphysema, we observed an accumulation of activated AT2s in the lung, associated with an overexpression of $p16^{INK4a}$ (p16), a cell cycle inhibitor known to influence stem cell fate. Deletion of p16 promoted the transition of AT2 into alveolar type 1 (AT1) cells, resulting in tissue regeneration in both mice and alveolar organoids. Pharmacological targeting of the p16 pathway using senolytic agents recapitulate this regenerative effect, further supporting the role of p16 as a key brake on epithelial plasticity. These findings demonstrate that alveolar epithelial cell dysfunction can be reversed by p16 deletion or by eliminating $p16^{+}$ cells, thereby reactivating the AT2-to-AT1 transition and promoting endogenous alveolar regeneration. This work identifies the p16 pathway as a promising therapeutic target for restoring damaged alveoli in emphysema.

Introduction

Pulmonary emphysema is a major component of chronic obstructive pulmonary disease (COPD) characterized by progressive destruction of alveoli. and is a leading cause of irreversible chronic respiratory failure. Because no current therapy can restore the alveolar architecture, identifying the mechanisms that enable regeneration of the lung structure in patients with emphysema is of critical importance.

Damaged tissues are repaired by progenitors that are activated during injury. In the alveolar epithelium, a tissue with relatively low renewal capacity, alveolar type 2 epithelial cells (AT2) are one of the main alveolar epithelial progenitor cells, which proliferate and differentiate into alveolar type 1 epithelial cells (AT1)[1]. Recent studies have revealed substantial heterogeneity within the alveolar epithelium, identifying distinct subpopulations of AT2 and intermediate transitional states that orchestrate regeneration[2–4]. AT2 stem cell dysfunction, characterized by impaired progression through these transitional states toward mature AT1, can arise from the combined effects of aging, cumulative environmental insults and genetic predisposition. This dysfunction initiates maladaptive cascades and contributes to the pathogenesis of several alveolar diseases, most notably pulmonary fibrosis[2,5–7]. However, whether similar defects in transitional epithelial populations underlie the impaired regenerative response in emphysema remains poorly understood.

A subset of these transitional epithelial states, particularly Krt8+ alveolar differentiation intermediates (ADI), exhibit an upregulation of senescence-associated genes including *Cdkn2A,* which encodes the cell cycle inhibitor p16^{INK4a} (p16). In emphysema, prior evidence has implicated AT2 in an apoptosis - proliferation imbalance skewed toward apoptosis [8], along with increased expression of senescent markers [9,10]. We previously demonstrated in a neonatal disease model that deletion of p16 or ablation of p16 positive cells promoted the recruitment of lipofibroblasts within the AT2 stem cell niche and enhanced alveolar regeneration from early life into adulthood[11]. However, whether targeting p16 in alveolar epithelial cells can similarly restore the regenerative capacity in adult-onset diseases such as emphysema remains unknown.

Here, we hypothesize that epithelial stem cell dysfunction is a key driver of the persistent alveolar destruction in emphysema and that targeting p16 could restore regeneration in the diseased lung. Using an elastase-induced mouse model of emphysema together with human and mouse-derived alveolar organoids, we found that alveolar epithelial stem cell dysfunction

marked by p16 overexpression, and accumulation of activated AT2 cells characterized by elevated expression of *Lcn2* and *Lrg1,* contributed to emphysema pathogenesis by impairing lung regeneration. Genetic deletion of p16 reversed this dysfunction, reduced activated AT2 accumulation, and restored alveolar regeneration *in vivo* and in organoid cultures. Moreover, pharmacological clearance of p16^{+} senescent cells using senolytic agents also restored epithelial function and ameliorated emphysema. Together, our findings identify p16-driven epithelial stem cell dysfunction as a central mechanism of emphysema progression and establish targeting p16^{+} cells as a potential regenerative therapeutic strategy in chronic lung disease.

Results

Alveolar epithelial stem cell dysfunction in elastase-induced emphysema is characterized by an increase in activated AT2 cells

To investigate epithelial cell alterations in emphysema, adult mice received a single intratracheal instillation of elastase, resulting in irreversible alveolar destruction. This was evidenced by a significant increase in the mean linear intercept (MLI) at day 21, which persisted through day 150 post-injury (**Fig. 1A-C**). To assess whether sustained alveolar damage was associated with impaired epithelial progenitor cell function, organoid cultures were established using MACS-sorted EpCAM^{+} epithelial from PBS-treated control or elastase-treated emphysematous lungs, co-cultured with primary lung fibroblasts. Notably, organoid formation was markedly reduced in both number and size at day 14 and 21 when EpCAM^{+} cells were derived from emphysematous lungs compared to controls (**Fig. 1D-E** and **Supplementary Fig. 1A)**, indicating that emphysema is associated with diminished indicating that emphysema is associated with diminished epithelial regenerative capacity in this *ex vivo* model. We next evaluated organoid formation using human AT2 cells. Primary AT2 were isolated by magnetic sorting of HT2-280-positive cells from lung explants of emphysematous and non-emphysematous patients (**Fig.1F, Supplementary Fig. 1B**) and co-cultured them with primary fibroblasts derived from different donors, emphysematous and non-emphysematous.

To determine the clinical factors associated with the number and size of the organoids as surrogate of the regenerative capacity of the alveoli, we performed an unsupervised cluster analysis including the following parameters for both AT2 and fibroblasts patients: number and size of the organoids, age, body mass index, level of smoking (pack-years), CT scan

emphysema score[12] and lung function parameters (FEV1, DLCO, residual volume (RV), total lung capacity (TLC), FEV1/FVC). We observed a cluster combining a smaller number and size of organoids associated with AT2 obtained from patients with higher levels of emphysema and lower lung function parameters (DLCO, FEV1) (**Fig. 1 G-H**). However, we did not observe an overlap between organoid size and number with the clinical characteristics of patients from whom fibroblasts were obtained, suggesting that emphysematous AT2 may be the main driver of organoid formation variation (**Supplementary Fig.1C**). We next paired emphysematous and non-emphysematous AT2 co-cultivated with the fibroblasts of the same donor. In paired cultures of emphysematous versus non-emphysematous AT2 co-cultivated with autologous fibroblasts (n = 18 pairs), emphysematous AT2 yielded significantly fewer organoids (**Fig. 1I**).

To further elucidate the cellular and molecular programs underlying this emphysema-associated impaired epithelial progenitor function, we performed single-cell RNA sequencing (scRNAseq) of FACS-sorted $CD31^{-}CD45^{-}EpCAM^{+}$ cells isolated from mouse lungs at day 21 (D21) and day 150 (D150) post-elastase or PBS treatment (**Fig. 1J-N, Supplementary Fig. 1D)**. After quality control filtering, we recovered a total of 31,172 epithelial cells at the different time points, encompassing all major alveolar (AT2, proliferating AT2 and AT1 cells), and airway epithelial cell types (ciliated, goblet and club cells). Within the *Sftpc*+ cells, subcluster analysis identified three AT2 cell subpopulations: classical AT2 cells expressing canonical markers (*Sftpc, Etv5, Cxcl15*), a *Sftpc*+ AT2 cells subset expressing *Lrg1*, *Lcn2* and *Il33* labelled activated AT2, and a *Sftpc*+ population expressing *Areg, Krt8, Lgals3* labeled pre-alveolar differentiation intermediates (pre-ADI) (**Fig. 1L-M).** These two last AT2 subpopulation exhibited transcriptional similarity to previously described activated/primed AT2[3,4,13] and Krt8+ transitional alveolar epithelial cells/regenerative AT2 cells/DATPs respectively[3,14,15]. The similarity of these two subpopulations with activated AT2 and ADI was supported by matchSCore analysis with respective cell state marker genes from a bleomycin induced lung fibrosis RNAseq dataset (**Supplementary Fig. 1E**)[13,16]. Compositional analysis revealed a time-dependent increase in the activated AT2 population in emphysematous mouse lungs compared to control, with an even greater elevation observed at D150 than at D21, although the other sub-populations were not modified in the emphysematous lung, particularly pre-ADI and AT2 (**Fig. 1N).** To determine whether this population is not specific to our model, we tested whether this increase of activated AT2 may be also observed in another model of mouse emphysema by performing gene signature scoring. We re-analyzed a publicly available scRNA-seq dataset of mice developing emphysema after 6-month cigarette smoke exposure[17].

Similarly, we detected an enrichment of activated AT2 signature in the smoke-exposed lungs compared to controls (**Supplementary Fig. 1F)**. To assess whether activated AT2 cells are also increased in human diseased lungs, we applied our mouse activated AT2 cell signature to two publicly available single-cell RNA-seq datasets from COPD patients[18,19]. This analysis revealed elevated expression of the signature in COPD-related emphysema in both population (**Supplementary Fig. 1G-H**). Altogether these results suggest strongly that accumulation of activated AT2 and alveolar epithelial dysfunction is an important feature of emphysema.

Alveolar epithelial stem cell dysfunction in elastase-induced emphysema is associated with p16 overexpression.

To decipher the molecular mechanisms contributing to impaired AT2 function and differentiation in emphysema, we performed differential gene and pathway analysis in the whole populations of AT2 cells (*Sftpc*$^+$ cells) obtained in the single-cell RNAseq analysis. Regarding different gene expressions, among the 20 top differentially expressed genes in elastase compared to PBS-treated AT2 cells, at both early and late time points, were genes that characterized activated AT2 such as *Lcn2*, *Lrg1 (***Fig 2A-B**). Among these overexpressed genes after elastase instillation were members of the uPAR family *Ly6a* and *Ly6i.* Moreover, among the genes modulated commonly at early and late time point were genes involved in cell cycle progression such as *Ccnd2* and *Cdca7* (with at early time point *Fos* and *Fosb*). Several of these overexpressed genes are involved in immune response and inflammation (*lLcn2, Lrg1, Cxcl17, Ly6i, Ly6a, Cd14, Ccl33*) (**Fig. 2A-B**). Pathway analysis shows an enrichment after elastase instillation at early and late time points for inflammatory signaling such as Interferon α and γ response, TNFα signaling hallmark (**Supplementary Fig. 2A**). Hypoxia, oxidative phosphorylation and reactive oxygen species pathways hallmarks that have been described as regulators of activated AT2 differentiation[3] were upregulated in elastase instilled lung (**Supplementary Fig. 2A**). Factors previously described to regulate activated AT2 such as factor Tfcp211 (YAP/Taz) or epithelial β1 integrins were not in the top gene modulated by elastase instillation at the different time points. Senescence activation and dysregulation of cyclin-dependent kinase pathways were detected across all AT2 subpopulations in elastase-injured lungs. We assessed validated senescence scores[20] and cell cycle pathway activity in AT2, pre-ADI, and activated AT2 cells over time following elastase instillation (**Fig. 2C-D**). Senescence scores were predominantly elevated in activated AT2 and pre-ADI cells, with elastase further amplifying this effect (**Fig. 2C-D**). Concurrently, expression of E2F targets,

G2/M checkpoint, and mitotic spindle genes was reduced across all subpopulations (**Fig. 2D**). Given that p16 is a key regulator of both senescence and cell cycle arrest, we hypothesized it may contribute to epithelial dysfunction in emphysema. While Cdkn2a transcripts were undetectable by scRNA-seq, immunostaining revealed increased numbers of p16^{+} AT2 cells in the alveolar walls of elastase-treated mice compared to controls at all time point (**Fig. 2E–F**).

p16 deletion induces alveolar regeneration and reverses epithelial stem cell dysfunction in emphysema

To assess whether p16 overexpression contributes to impaired epithelial repair, we evaluated lung morphology in WT and p16$^{-/-}$ mice at day 21 after elastase instillation (established emphysema), and at days 90 and 150 (persistent emphysema) (**Fig. 3A**). At day 21, MLI was comparable between WT and p16$^{-/-}$ mice following elastase, indicating that p16 deficiency does not prevent initial alveolar destruction (**Fig. 3B–C**). However, by day 90, p16$^{-/-}$ mice showed a significant reduction in MLI, indicating spontaneous improvement of emphysema. This regeneration persisted through day 150 (**Fig. 3B–C**).

To assess epithelial progenitor function, we generated alveolar organoids using EpCAM^{+} cells from WT or p16$^{-/-}$ mice 21 days after elastase injury, co-cultured with WT lung fibroblasts. P16 deletion significantly increased organoid number and size (**Fig. 3D-E**), indicating restored epithelial stem cell function in emphysema. To test whether p16 deletion enhances epithelial progenitor potential in the absence of injury, EpCAM^{+} cells from PBS-treated WT or p16$^{-/-}$ mice were co-cultured with WT fibroblasts. While organoid numbers were unchanged, organoid size was increased with p16$^{-/-}$ cells (**Fig. 3F-G**). Finally, to assess whether fibroblasts contribute to p16-mediated regeneration, we generated organoids using EpCAM^{+} cells from elastase-instilled mice co-cultured with elastase-instilled fibroblasts with or without the deletion of p16. The p16 deletion in fibroblasts led to a slight, non-significant increase in organoid formation, although overall organoid numbers were low (**Supplementary Fig. 3A-B)** and fibroblasts p16$^{-/-}$ do not exhibit a higher proliferative potential compared to WT (**Supplementary Fig. 3C**). Immunohistochemistry at day 90 showed no differences in adipose differentiation-related protein (ADRP) staining between groups, excluding a role for lipofibroblasts in the regeneration process (**Supplementary Fig. 3D–E**). Together, these findings indicate that p16 deletion promotes spontaneous late alveolar regeneration primarily through intrinsic epithelial mechanisms, rather than fibroblast-mediated effects. This suggests

that p16 overexpression sustains epithelial stem cell dysfunction in emphysema, and that its deletion may reactivate endogenous alveolar repair.

Alveolar regeneration due to p16 deletion involves decrease of activated AT2

We next examined the characteristics of the cells implicated in this regenerative p16-dependent phenotype in the elastase-induced emphysema model. By immunofluorescence staining, we observed in p16$^{-/-}$ mice compared to WT mice after elastase instillation an increase of AT2 at D21 (**Supplementary Fig. 3F)** and of SpC^{+}/KRT8^{+} (**Fig. 3H-J)**. Interestingly, we did not find any difference between emphysematous and non-emphysematous lung in human regarding AT2 SpC^{+}KRT8^{+} cells and SpC^{-} KRT8^{+} KRT17^{+} transitional cells (**Fig. 3K-M**). To dissect the involvement of the different AT2 subpopulations in the regeneration observed in case of p16 deletion, we performed a scRNAseq analysis on EpCAM^{+}CD31^{-}CD45^{-} cells at D21 and D150 after elastase instillation in WT and p16$^{-/-}$ mice (**Fig. 3A**). After quality controls, we recovered a total of 59,275 epithelial cells. The previously described AT2 subpopulations were also observed in the lung of p16$^{-/-}$ mice after PBS or elastase instillation at the two time points (**Fig. 3N-O, Supplementary Fig 3G**). The p16 deletion in elastase-injured mice promoted a reduction of activated AT2 compared to WT elastase mice and reached the level of WT control mice at D21 and D150 (**Fig. 3P**).

To investigate AT2 to AT1 differentiation trajectories we performed cell state trajectory analysis using RNA velocity (scVelo) and summarized lineage relationships with partition-based graph abstraction (PAGA). RNA velocity analysis predicted a differentiation trajectory of AT2 cells toward both activated AT2 and pre-ADI cells in elastase-injured lungs (**Supplementary Fig. 3H**). These trajectories differ from those observed in p16$^{-/-}$ mice, where activated AT2 cells progress toward AT2, pre-ADI, and AT1 cells, consistent with normal lung regeneration (**Supplementary Fig. 3I**). To investigate mechanisms underlying the reduction of activated AT2 cells in p16$^{-/-}$ mice, we performed gene and pathway analysis. At day 150, 15 of the top 20 genes upregulated by elastase injury in WT mice were downregulated in p16$^{-/-}$ mice, including *Lcn2*, *Lrg1*, *Cd14*, *Cxcl17*, *Id3*, *Dmkn*, *Phgr1*, *Ptges*, *Clu*, *Tacstd2*, *Slc26a4*, and *Malt1* (**Fig. 3Q**). Among the top 20 downregulated by elastase, 7 were upregulated in p16$^{-/-}$ AT2: *CCnd2*, *Sik2*, *Auts2*, *Ttn*, *Hsph1*, *Hspa8, Bex4.* These gene expression changes further support a critical role for p16 in sustaining elastase-induced emphysema at late time points. Pathway analysis shows that the most enriched pathway was the GTPase pathway, mainly at day 150 (**Fig. 3R**). Several pathways involved in AT2 proliferation and differentiation were

enriched in p16$^{-/-}$ mice (Wnt and Notch signaling, Type 1 pneumocytes differentiation, epithelial cell development) or in repair process (wound healing, regulation of pluripotency of stem cells). Cell cycle pathways were also upregulated, G2/M and G1/S transition, associated with several pro survival pathways (MTOR signaling, PI3K-Akt signaling, longevity regulating pathways). Of note, cellular senescence and p53 signaling pathways enrichment appears to be restricted to day 21, suggesting dynamic changes of senescence throughout the regeneration process in case of p16 deletion. Altogether, these results highlight that p16 deletion in AT2 reverses epithelial dysfunction in this model of lung destruction in adult mice and restores the AT2 cell sub populations in proportions.

p16 deletion induces alveolar regeneration without aberrant process of fibrosis or cancer

We next questioned if this regenerative process could be in part aberrant with the development of fibrosis or lung cancer[21]. We thus quantified septal thickness (**Supplementary Fig. 4A)**, collagen deposition **(Supplementary Fig. 4B**), and myofibroblasts content **(Supplementary Fig. 4C**) as markers of lung fibrosis. These markers were transiently increased at D90 in p16$^{-/-}$ mice as compared to WT animals and returned to the baseline level at D150, confirming the absence of an aberrant remodeling process and suggesting an important step in the regenerative process involving fibrogenesis. At histologic level, we did not observe any pulmonary neoplastic process during the follow-up of mice with a deletion of p16 until D150. Moreover, a CT scan was performed 1 year after elastase instillation on the lungs of WT and p16$^{-/-}$ mice. We did not observe any tumors, also excluding a long-term process of lung carcinogenesis associated with p16 deletion and emphysema (**Supplementary Fig. 4D**). P53 is a crucial tumor suppressor that suppresses lung adenocarcinoma development from AT2. At the gene level, the emphysematous destruction was associated at D21 with an elevation of p53 and p21 mRNA (**Supplementary Fig. 4E-F**). Altogether, these results show that p16 deletion triggers spontaneous alveolar regeneration in emphysema once lesions are established without the occurrence of fibrosis or lung cancer.

Elimination of p16+ cells by senolytics restores epithelial function and reverses emphysema

To confirm that deletion of p16 modulates senescence in our mice model of emphysema, we quantified senescence by analyzing senescence-associated βgalactosidase (SA-βgal) staining

in lungs from WT and p16$^{-/-}$ mice following elastase injury (**Fig. 4A**). p16$^{-/-}$ lungs showed reduced SA-βgal staining at day 21 (**Fig. 4B, C**). Similarly, organoids derived from EpCAM^{+} cells of p16$^{-/-}$ lungs had fewer SA-βgal–positive structures compared to WT (**Fig. 4D, E**).

To evaluate the therapeutic potential of eliminating p16^{+} cells and reducing senescence, we tested the senolytics Dasatinib and Quercetin in both an *in vivo* emphysema model and organoid assays. WT mice with established emphysema were treated from day 21 to 90 (**Fig. 4F**). Senolytic treatment significantly reduced MLI (**Fig. 4G-H**), increased AT2 cell numbers, and elevated the proportion of pre-ADI cells (SpC^{+}/KRT8^{+}) compared to vehicle-treated controls (**Fig. 4I–K**). In parallel, we treated with senolytics organoids generated by co-culturing WT fibroblasts with EpCAM^{+} cells from emphysematous WT lungs (**Fig. 4L**). Senolytics reduced SA-βgal staining in organoids (**Fig. 4M-N**) and significantly increased both organoid number and size, indicating improved epithelial progenitor function (**Fig. 4O-P**). Together, these results confirm that targeting p16^{+} senescent cells can restore epithelial function and promote alveolar regeneration in emphysema.

DISCUSSION

In this study, we show that alveolar epithelial stem cell dysfunction in elastase-induced emphysema is associated with an accumulation of activated AT2 cells and p16 overexpression. Deletion of p16 restores epithelial stem cell function and promotes alveolar regeneration. Finally, elimination of $p16^+$ cells using senolytics reverses both epithelial dysfunction and emphysematous lung destruction. These results suggest that activated AT2 cells may play a key role in the lack of repair in emphysema and establish p16 as a major regulator of both their behavior and the failure of epithelial repair. They also highlight promising therapeutic avenues to reverse lung destruction through senescence-targeted interventions

The exact role of the activated AT2 cells remains to be fully defined, as their phenotype and trajectory may vary depending on the model of injury. In bleomycin-induced injury, RNA velocity analyses[4] have identified a transitional population between AT2 and AT1 cells, referred to as ADIs or damage-associated transient progenitors (DATPs)[3]. These cells are thought to represent a necessary step in epithelial regeneration. In our model of elastase-induced emphysema, activated AT2 cells accumulate without evidence of progression toward AT1 differentiation. Indeed, our trajectory analysis indicates that, in emphysema, differentiation toward the activated AT2 state may become a dead-end, failing to progress toward differentiation. In contrast, *p16* deletion restores the continuity of the differentiation pathway, allowing progression toward pre-ADI and AT1 states without aberrant fibrosis or cancer. These findings raise the possibility that, in emphysema, activated AT2 cells reflect a blocked or maladaptive differentiation state, distinct from functional ADI/DATP intermediates. Hu *et al.* recently discovered a club-cell derived emphysema enriched AT2 sub-populations with poor alveolar progenitor potential in both humans (asATII) and mouse emphysematous lungs (ATII-6) that is marked in mice by *Ly6i, Lcn2, Slc26a4,* genes that were also upregulated in our activated AT2 cell population[19]. However, the role of activated AT2 cells in emphysema, their full integration within the stem cell niche, as well as their interactions with distal airway cells, remains to be fully elucidated.

The precise mechanisms by which p16 interferes with AT2 cell differentiation remain unclear. Although YAP/TAZ signaling and the transcription factor Tfcp2l1 have been implicated in activated AT2 regulation[22,23], we did not observe their modulation in our single-cell pathway analyses, and no established link between p16 and these pathways exists to date. GTPases pathway could play a central role in our tissue regeneration since p16 deletion induced repair

is associated with a strong increase of these pathways. GTPases are known to promote epithelial cell proliferation and survival through activation of mitogenic pathways such as MAPK/ERK and PI3K/AKT[24]. These pathways are essential for stem cell expansion and repair following injury. In addition, GTPases integrate extracellular signals, including mechanical signals, to modulate regenerative responses (25–27)[25–27], positioning them as key regulators of epithelial renewal that contribute to active maintenance of AT1 cell identity[27].

Previous studies have shown that p16 is overexpressed in emphysema, both in mouse models and in humans[9,28,29]. We demonstrated that either genetic deletion of p16 or pharmacological elimination of $p16^+$ cells is associated with a restoration of lung architecture in a curative manner in emphysema at a late time point after elastase instillation. We had previously demonstrated that p16 deletion or elimination of $p16^+$ cells in the post-natal hyperoxia model of bronchopulmonary dysplasia induced a catch-up alveolar growth between childhood and adulthood[11]. In that model, the restoration of alveolar structure at adulthood was mainly associated with an increase in lipofibroblasts adjacent to AT2 cells after p16 deletion or $p16^+$ cells removal. This phenomenon was not observed in the adult emphysema model, suggesting that the impact of p16 on alveolar repair process may differ depending on age. A common feature of both models is that late time points are required after the initial injury to unmask the regenerative effect of p16 deletion. These results highlight that targeting p16 and cellular senescence in alveolar epithelial cells could be a promising approach to regenerate the lung in emphysema without inducing an aberrant fibrotic of oncogenic processes. Harnessing tissue regeneration in this context could open a novel therapeutic window for patients with severe and irreversible lung disease.

Methods

Animals

C57BL/6J mice (8-14 weeks) were housed in a pathogen-free barrier environment throughout the study (12 h light/dark cycle with access to food and water ad libitum). The Institutional Animal Care and Use Committee approved experimental procedures on mice (APAFIS#25872-2020060317048060v3). The p16$^{INK4a-/-}$ mice were kindly provided by Anton Berns (Netherlands Cancer Institute, Amsterdam) [30].

Elastase-induced emphysema

Mice were randomly assigned into PBS or elastase groups. The lung injury was induced by an intra-tracheal instillation of a single dose administration of 2 UI of elastase (Elastin Products Company) diluted in sterile 50 µL of PBS. The control group was treated with sterile PBS only. Mice were sacrificed at D21, D90 and D150 after instillation. All analysis realized in the lung of these mice were done blinded.

Morphometry

Murine lungs were perfused with cannula at 25 cmH2O for 30 min and fixed in 4% paraformaldehyde. Next, they were embedded in paraffin and sectioned at 5 µm thickness. Hematoxylin/eosin staining was performed according to standard procedures. Ten digital photomicrographs at 20X were performed in the histological section. The standard morphometric methods were used, that is, counting the number of points touching the alveolar parenchyma (point counting) and the number of intersections between the graduated lines and the elastic fibers (mean linear intercept).

Lung elastic fiber status and collagen content

Elastic fiber morphology and length were evaluated using Weigert's technique. Collagen content was evaluated after red Sirius staining.

Senescence-associated β-galactosidase staining

Senescence-associated β-galactosidase staining was performed in whole-amount lungs using the Senescence β-Galactosidase Staining Kit (Cell Signaling©). Briefly, whole-amount was fixed at room temperature, for 45min, with a fixative solution, washed three times with PBS,

and incubated overnight at 37°C with the Staining Solution containing X-gal in N-N-dimethylformamide (pH 6.0). Whole-amount lungs were subsequently dehydrated with two consecutive steps in 50% and 70% ethanol and embedded in paraffin for serial sectioning. Sections were counterstained with nuclear fast red.

Immunofluorescence staining

We prepared and stained formalin-fixed, paraffin-embedded 5-µm-thick lung sections using standard procedures. Briefly, sections were deparaffinized through graded Xylen then alcohol and washed in PBS. Immunofluorescence staining was performed using anti-proSpC (Abcam, ab90716 1/500), anti α-smooth muscle actin (Abcam, ab5694, 1/200), anti-KRT8 (DSBH, TROMA-I, 4 µg / mL), anti-KRT17 (Santa Cruz Biotech, sc-393002, 1/100), anti-ADRP (Progen GP42, 1/400), anti-p16 (Abcam, ab54210, 1/200), anti-LRG1 (Santa Cruz sc-390920). Secondary antibodies were from life technologies. Nuclei were counter-stained using prolonged anti-fade reagent with DAPI (Life Technologies©, E1740384).

Microscopes

Briefly, randomized images were acquired (Axiophoto; Carl Zeiss MicroImaging equipped with a digital camera AxiocamHRc; Carl Zeiss MicroImaging). Image acquisition was performed using a fluorescence microscope (Axioimager M2; Zeiss) at X40. The quantification of the different staining was performed using Image J (color deconvolution).

RNA extraction and gene expression analysis

RNA extraction from sorted murine lung cells was done using RNeasy kit (Qiagen©) and quantitative real-time PCR (*q*PCR) analysis was performed using Quant Studio 6. Data were presented as expression relative to hypoxanthine-guanine phosphoribosyl transferase 1 (Hprt 1).

Mouse alveolar organoids

Primary lung fibroblasts were isolated for mouse lungs after enzymatic and mechanical dissociation. Lungs were perfused with ice-cold PBS through the right ventricle, excised and minced in small pieces that were placed in dispase (5 UI/ml, Corning), type 1 collagenase (X) and placed in a Gentlemacs Octodissociator (Miltenyi) for 45 min) at 37°C. After digestion, the solution was filtered in 70- and 40-micron strainer (Corning), washed and plated in

Dulbecco's Modified Eagle's Medium/F12 (Invitrogen) supplemented with anti-anti (Thermofischer) and 10 FBS (Hyclone). Six hours post-plating, supernatant with non-adhesive cells was removed. The purity of culture was assessed by staining for vimentin and the absence of staining for aSMA, CD31, CD45 and cytokeratin. At the 2nd passage, 50000 fibroblasts were coculture with 20 000 EpCAM^{+} cells. These cells were obtained by the same protocol of digestion followed by a negative (Ter119-CD31-CD45-LNGFR-CD16/32-CD90) than a positive magnetic bead sorting (CD326^{+}). Cells were resuspended in SABM (small airway basal medium supplemented with vial except epinephrin) and mixed with matrigel (Corning) at a ratio of 1/1 and added to a 24-well transwell filter inserts with 0.4 microns pore (Corning) in a 24 well tissue culture plate containing 500 µL of medium (SABM). The medium was supplemented with Rock inhibitor for the 48 first hours then changed every 2 days. Cultures were incubated at 37°C in a humidified incubator (5% CO2).

Human alveolar organoids

Fibroblasts and AT2 cells are obtained from lung tissue from patients undergoing lung surgery for lung cancer (CoStemCells study, ClinicalTrials.gov NCT05227547). Primary lung fibroblasts were isolated by the explant's technique. AT2s were obtained by magnetic bead sorting using anti-HT2-280 antibody (Terrace biotech). A suspension of 50 000 fibroblasts and 5000 AT2 were mixed with matrigel (Corning) at a ratio of 1/1 and added to a 24-well transwell filter inserts with 0.4 µm pore (Corning) in a 24-well tissue culture plate containing 500 µL of medium (SABM, Lonza). The medium was supplemented with Rock inhibitor for the first 48 hours then changed every 2 days. Cultures will be incubated at 37°C in a humidified incubator (5% CO2). The number of organoids (colony forming efficiency) and the size were analyzed on day 14 post-plating.

Senolytic drug treatments

Dasatinib (D) and quercetin (Q) were used *in vitro* at 5 µM and 50 µM respectively, and DMSO was used as a control. For the *in vivo* experiment, senolytics were delivered by oral gavage every five days at 5mg/kg for Dasatinib and 50 mg/kg for Quercetin from D21 to D90 after elastase instillation in 10% propylene glycol (vehicle).

Single-cell RNAseq analysis

For scRNA-seq, a single-cell suspension was prepared from the EpCAM^{+}CD31^{-}CD45^{-} cells (Anti-CD326: 118213 1/100, Anti-Ter119: 116208, Anti-CD31: 102418 1/100, Anti-CD45: 103155 1/100, DAPI: 422801 1/300, Biolegend) sorted by FACS from the lungs of 2 mice pooled for each group at day 21 and 150 following PBS or elastase instillation in WT or p16$^{-/-}$ mice. Approximately 20,000 cells were loaded onto a 10x Genomics Chip G with Chromium Single Cell 3′ v3.1 gel beads and reagents (3′ GEM v3.1, 10x Genomics). Single index libraries were generated following the manufacturer's protocol (10x Genomics, CG000204_RevD). The scRNA-seq libraries were pooled and sequenced using a NovaSeq 6000 instrument [read 1: 28 base pairs (bp), Index1 8bp/ Index2 0bp/read2 55bp]. Count matrices were produced using the Cellranger computational pipeline (v7.0.1, STAR v2.7.2a), with reads aligned to the mm10 mouse reference genome (GRCm38). After preprocessing and quality control, scRNA-seq data were analyzed using the Python package Scanpy (> v1.8.2) following the current Single Cell Best Practice Guidelines: https://www.sc-best-practices.org/preamble.html.

Preprocessing and analysis of epithelial cells scRNA-seq data

To reduce the impact of batch correction on downstream annotations, we first processed and annotated the WT mouse datasets independently, and only afterward integrated them with the p16$^{-/-}$ samples. During quality control, genes with fewer than one count or expressed in fewer than one cell were excluded. Cells with mitochondrial transcript proportions of 10% or higher were also removed. Doublets were identified using Scrublet [31] on each sample separately, and ambient RNA contamination was corrected with soupX [32], with the contamination fraction manually set to 0.4. Normalization was performed using scran's size factor approach, based on Louvain clustering (resolution = 1.0). Finally, log transformation was applied with the pp.log1p() function in Scanpy.

Highly variable genes (HVGs)

For each sample, we identified the top 4000 highly variable genes and considered a gene as globally variable only if it was consistently variable across at least four samples. After excluding cell cycle–associated genes, 3170 HVGs remained. These genes were then used as input for Principal Component Analysis (PCA), followed by the construction of a k-nearest neighbor (kNN) graph based on the first 50 principal components. Clustering was performed using the Leiden algorithm, and clusters were annotated with reference to canonical marker genes. Initially, we carried out a coarse annotation of the dataset and extracted an EPCAM^{+} epithelial compartment, which included both alveolar and airway cell types, while filtering out

contaminants and poor-quality cells. We then repeated HVG selection, PCA, and clustering to refine the annotation and resolve four distinct epithelial lineages.

Differential gene expression testing (DGE)

Differential expression analysis was carried out on SCRAN-normalized counts using diffxpy (v0.7.4). A Wald test with default settings was applied to all genes detected in at least five cells. Genes were considered significantly differentially expressed when they showed a log2 fold change greater than 0.5 and an FDR-adjusted *p*-value below 0.05.

Gene signature scoring

We defined an activated AT2 gene signature consisting of *Scd1, Lrg1, Lcn2, Itih4, Hdc, Mfsd2a, Ptges, Cxcl17, H2-Q7, 9530077C05Rik, Proz, Phgr1, Alkal1, Slc5a1, Dmkn,* and *Fgg*. This set was derived from the integrated dataset based on the following criteria: FDR-adjusted *p*-value < 0.05, log2 fold change > 2, and expression detected in less than 25% of the background population. Signature scores were computed in Scanpy using the sc.tl.score_genes() function (default settings), by subtracting the mean expression of randomly selected control genes from the mean expression of the signature genes.

Enrichment analysis of gene cluster

Enrichment Analysis of gene cluster was performed in R using the clusterProfiler package, with libraries from: 'MSigDB_Hallmark_2020', 'GO_Biological_Process_2021', 'GO_Cellular_Component_2021', 'GO_Molecular_Function_2021', 'Reactome_2016', 'KEGG_2021_Human'. Gene sets were considered enriched in the respective signature at a statistically significant level if the FDR-corrected p-value was below 0.05.

Trajectory inference analysis

Trajectory inference analysis and fate mapping was conducted using the Python packages scVelo (version 1.10.1) and CellRank (version 2.0.4). We inferred the splicing kinetics of all genes and estimated RNA velocity using the dynamical model in scVelo. We confirmed this finding by inferring the trajectory of AT2 sub-populations using Partition-Based Graph Abstraction (PAGA).

Re-analysis of publicly available single-cell RNAseq data

We compared our scRNA-seq data against publicly available COPD patients (GEO GSE173896[18] and GEO GSE222374[19]), elastase mice (GEO GSE222374)[19] and cigarette smoke exposed mice (GEO GSE151674)[17]. To compare our gene signature scores for activated AT2 in mouse across health conditions in human COPD and cigarette smoke exposed mice, we calculated the scores for each AT2 sub-populations from these articles, and after combined them, we used the function sc.get.obs_df before to plot the results. The results were tested for statistical significance using either a Kruskal-Wallis test for multiple or Mann Whitney test for two group comparisons.

Agglomerative hierarchical clustering analysis

Agglomerative hierarchical clustering analysis was used to identify if clinical, functional, and radiological characteristics of control and emphysematous patients are linked to the capacity of their AT2 cells or fibroblasts to form organoids. This analysis combines similar subjects based on selected features (the number and size of organoids formed, patient age (in years), smoking history (in pack-years), the proportion of emphysema as quantified by chest computed tomography, the FEV_1/FVC ratio (%), FEV_1 (%), RV (%) and DLCO (%) to create homogeneous clusters of control and emphysematous patients characterized by an overall similar functional profile. Hierarchical clustering was performed on standardized raw (e′ septal and e′ lateral) or log-transformed (all other variables) values, depending on the normality of distribution, based on Euclidean distance as the similarity metric and using the Ward linkage approach. All clustering was performed blinded to clinical data.

Statistical analysis

Student's t-test (unpaired, two-tailed) was used to compare the means of two groups and two-way ANOVA was used to compare the means of multiple groups. Data were presented as mean values ± SEM, and results were considered statistically significant if $p < 0,05$.

References

1. Barkauskas, C. E. *et al.* Type 2 alveolar cells are stem cells in adult lung. *J. Clin. Invest.* **123**, 3025–3036 (2013).
2. Kobayashi, Y. *et al.* Persistence of a regeneration-associated, transitional alveolar epithelial cell state in pulmonary fibrosis. *Nat. Cell Biol.* **22**, 934–946 (2020).
3. Choi, J. *et al.* Inflammatory Signals Induce AT2 Cell-Derived Damage-Associated Transient Progenitors that Mediate Alveolar Regeneration. *Cell Stem Cell* **27**, 366–382.e7 (2020).
4. Strunz, M. *et al.* Alveolar regeneration through a Krt8+ transitional stem cell state that persists in human lung fibrosis. *Nat. Commun.* **11**, 3559 (2020).
5. Lehmann, M. *et al.* Senolytic drugs target alveolar epithelial cell function and attenuate experimental lung fibrosis ex vivo. *Eur. Respir. J.* **50**, (2017).
6. Kathiriya, J. J., Brumwell, A. N., Jackson, J. R., Tang, X. & Chapman, H. A. Distinct Airway Epithelial Stem Cells Hide among Club Cells but Mobilize to Promote Alveolar Regeneration. *Cell Stem Cell* **26**, 346–358.e4 (2020).
7. Basil, M. C. *et al.* Human distal airways contain a multipotent secretory cell that can regenerate alveoli. *Nature* **604**, 120–126 (2022).
8. Calabrese, F. *et al.* Marked alveolar apoptosis/proliferation imbalance in end-stage emphysema. *Respir. Res.* **6**, 14 (2005).
9. Tsuji, T., Aoshiba, K. & Nagai, A. Alveolar cell senescence in patients with pulmonary emphysema. *Am. J. Respir. Crit. Care Med.* **174**, 886–893 (2006).
10. Alder, J. K. *et al.* Telomere dysfunction causes alveolar stem cell failure. *Proc. Natl. Acad. Sci.* **112**, 5099–5104 (2015).
11. Zysman, M. *et al.* Targeting p16INK4a Promotes Lipofibroblasts and Alveolar Regeneration After Early Life Injury. *Am. J. Respir. Crit. Care Med.* (2020) doi:10.1164/rccm.201908-1573OC.
12. Wang, Z. *et al.* Optimal Threshold in CT Quantification of Emphysema. *Eur. Radiol.* **23**, 975 (2012).
13. Gote-Schniering, J. *et al.* Single cell decomposition of multicellular aging programs associated with impaired lung regeneration. *bioRxiv* 2025.07.24.666371 (2025) doi:10.1101/2025.07.24.666371.
14. Wang, Z. *et al.* Enhanced glycolysis-mediated energy production in alveolar stem cells is required for alveolar regeneration. *Cell Stem Cell* **30**, 1028–1042.e7 (2023).
15. Wang, F. *et al.* Regulation of epithelial transitional states in murine and human pulmonary fibrosis. *J. Clin. Invest.* **133**, (2023).
16. Mereu, E. *et al.* Benchmarking single-cell RNA-sequencing protocols for cell atlas projects. *Nat. Biotechnol.* **38**, 747–755 (2020).
17. Conlon, T. M. *et al.* Inhibition of LTβR signalling activates WNT-induced regeneration in lung. *Nature* **588**, 151–156 (2020).
18. Watanabe, N. *et al.* Anomalous Epithelial Variations and Ectopic Inflammatory Response in Chronic Obstructive Pulmonary Disease. *Am. J. Respir. Cell Mol. Biol.* **67**, 708–719 (2022).
19. Hu, Y. *et al.* Airway-derived emphysema-specific alveolar type II cells exhibit impaired regenerative potential in COPD. *Eur. Respir. J.* **64**, (2024).
20. Saul, D. *et al.* A new gene set identifies senescent cells and predicts senescence-associated pathways across tissues. *Nat. Commun.* **13**, 1–15 (2022).
21. Konkimalla, A. *et al.* Transitional cell states sculpt tissue topology during lung regeneration. *Cell Stem Cell* **30**, 1486–1502.e9 (2023).
22. DiGiovanni, G. T. *et al.* Epithelial Yap/Taz are required for functional alveolar regeneration following acute lung injury. *JCI Insight* **8**, (2023).

23. Cardenas-Diaz, F. L. *et al.* Temporal and spatial staging of lung alveolar regeneration is determined by the grainyhead transcription factor Tfcp2l1. *Cell Rep.* **42**, 112451 (2023).
24. Crosby, L. M. & Waters, C. M. Epithelial repair mechanisms in the lung. *Am. J. Physiol.-Lung Cell. Mol. Physiol.* **298**, L715–L731 (2010).
25. Dupont, S. *et al.* Role of YAP/TAZ in mechanotransduction. *Nature* **474**, 179–183 (2011).
26. Shiraishi, K. *et al.* Biophysical forces mediated by respiration maintain lung alveolar epithelial cell fate. *Cell* **186**, 1478–1492.e15 (2023).
27. Wu, H. *et al.* Progressive Pulmonary Fibrosis Is Caused by Elevated Mechanical Tension on Alveolar Stem Cells. *Cell* **180**, 107–121.e17 (2020).
28. Amsellem, V. *et al.* Telomere dysfunction causes sustained inflammation in chronic obstructive pulmonary disease. *Am. J. Respir. Crit. Care Med.* **184**, 1358–1366 (2011).
29. Houssaini, A. *et al.* mTOR pathway activation drives lung cell senescence and emphysema. *JCI Insight* **3**, (2018).
30. Krimpenfort, P., Quon, K. C., Mooi, W. J., Loonstra, A. & Berns, A. Loss of p16Ink4a confers susceptibility to metastatic melanoma in mice. *Nature* **413**, 83–86 (2001).
31. Wolock, S. L., Lopez, R. & Klein, A. M. Scrublet: Computational Identification of Cell Doublets in Single-Cell Transcriptomic Data. *Cell Syst.* **8**, 281–291.e9 (2019).
32. Young, M. D. & Behjati, S. SoupX removes ambient RNA contamination from droplet-based single-cell RNA sequencing data. *GigaScience* **9**, (2020).

Author contributions

Conceptualization: BRB, MT, GT, MZ, CTDM, SL, JB, JGS, LB

Methodology: BRB, MT, GT, PAA, TDFC, MZ, CTDM, EA, MA, KS, HW, ML, JB, JGS, LB

Validation: BRB, MT, SL, FC, CJLS, YH, MK, ML, GD, JB, JGS, LB

Formal analysis: BRB, MT, GT, PAA, TDFC, MZ, EA, CJLS, YH, MK, ML, GD, JB, JGS, LB

Investigation: BRB, MT, GT, PAA, TDFC, MZ, CTDM, EA, MA, KS, HW, ML, JGS, LB

Data curation: BRB, MT, GT, JG, LB

Supervision: SL, FC, CJLS, ML, GD, JB, JGS, LB

Funding acquisition: BRB, MT, MZ, FC, GD, JB, LB

Writing—original draft: BRB, MT, CJLS, JGS, LB

Acknowledgment

This work was supported by a fellowship from INSERM and ARAIRLOR (BRB), UPEC doctoral school (MT), IMRB and Oxyvie (LB), Fondation pour la Recherche Medicale (FRM, LB) and Fondation du Souffle (LB). The authors thank members of Team Derumeaux and Team Lanone for their precious expertise and their help, Fanny Coulpier (Institut Mondor de Recherche Biomédicale, IMRB-INSERM U955) for her assistance in performing the single cell analysis, Slimani Lofti from Université de Paris, URP2496 Pathologies, Imagerie et Biothérapies Orofaciales et Plateforme Imagerie du Vivant (PIV) for CT scan images. The authors also thank Xavier Decrouy, Christelle Micheli (IMRB–INSERM U955, Créteil, France) and Adrien Lalot (animal facility). The assistance of Adeline Henry, Odile Ruckebusch and Aurélie Guguin (Installation de Cytométrie en Flux, IMRB-INSERM U955, Créteil, France). We sincerely thank William J. Zacharias (Cincinnati Children's Hospital) for his insightful guidance and generous advice regarding organoid generation. Finally, the authors thank Silvia Fre, Bruno Crestani, Philippos Mourikis and for their advice.

Competing interests

The authors declare no competing interests.

Legends

Figure 1: Alveolar epithelial dysfunction and accumulation of activated AT2 in mouse emphysema (A) Experimental design of organoid formation from epithelial cells ($EpCAM^+CD45^-CD31^-$) of mouse lungs from elastase-induced emphysema model. (B) Hematoxylin-eosin staining of lungs at D21, D90 and D150 post treatment of elastase to induce emphysema or PBS as a control (scale bar = 500 µm). (C) Quantification of mean linear intercept (MLI). (D) Representative images of organoids obtained from the coculture of $EpCAM^+$ from elastase and PBS treated mice and WT fibroblasts after 21 days of culture. (E) Colony forming efficiency (CFE %) and size (µm). (F) Experimental design of human alveolar organoid assay from the coculture of AT2 from control or emphysematous patients (n=16) with primary fibroblasts from control or emphysematous patients from different donors (n=8) and (G) Representative images of alveolar organoids formed at day 14. (H) CFE as a function of AT2 cell origin. Each data point corresponds to a co-culture of primary fibroblasts with AT2 cells from a patient without emphysema, compared to the culture of the same fibroblasts with AT2 cells derived from emphysematous tissue. (I) Cluster analysis of the number and size of organoids formed, patient age, smoking history (in pack-years), proportion of emphysema as quantified by chest computed tomography, FEV_1/FVC ratio (%), FEV_1 (%), and TLCO (%). Color intensity reflects the standardized (z-score) value of each variable, allowing visual comparison across patient subgroups, blue represents the lowest average values, and red the highest. FEV_1/FVC ratio (forced expiratory volume in 1 second / forced vital capacity), FEV_1 (forced expiratory volume in 1 second), FVC (forced vital capacity), RV (residual volume) DLCO (diffusion capacity of the lung for carbon monoxide). (J) Experimental design of single-cell RNAseq from epithelial cells ($EpCAM^+CD45^-CD31^-$) of mouse lungs from elastase-induced emphysema model (K) Uniform manifold approximation and projection (UMAP) of AT2 cells clustering depending on PBS or elastase treatment. (L) UMAP of Leiden subclustering of AT2 cells. (M) Dotplot of gene signature of clustered AT2 subpopulations. (N) Relative frequency of AT2 subpopulations depending on treatment and timepoints. *p = 0.05, **p = 0.01, ***p = 0.001, ****p = 0.0001 and ns = not significant

Figure 2: Alveolar epithelial stem cell dysfunction in elastase-induced emphysema is associated with p16 overexpression. Volcano plot of differentially expressed genes at D21 (A) and D150 (B) in AT2 cells of elastase mice compared to PBS. Significant features are

highlighted, with upregulated in red and downregulated in blue; non-significant features are shown in grey. (C) Dotplot of enrichment scores for three senescence-related gene sets (from[4,20]) and (D) three cell cycle-related gene sets (E2F targets, G2M checkpoint, Mitotic spindle) in AT2 subpopulations, depending on treatments and timepoints. (E) Immunofluorescence staining of Pro-SpC (red) and p16 (green) in PBS and elastase treated mice and (F) quantification of AT2 expressing p16 on all AT2 depending on treatments and timepoints. *p = 0.05, **p = 0.01, ***p = 0.001, ****p = 0.0001 and ns = not significant

Figure 3: p16 deletion induces lung regeneration and decrease activated AT2 in elastase treated mice (A) Experimental design of single-cell RNAseq on EpCAM^{+} cells from lungs of elastase-induced emphysema with WT and p16$^{-/-}$ mice. (B) Hematoxylin-eosin staining of WT and p16$^{-/-}$ lungs at D21, D90 and D150 injected with elastase (scale bar = 500 µm). (C) Quantification of mean linear intercept (MLI). (D) Representative images of organoids obtained with EpCAM^{+} from WT and p16$^{-/-}$ treated with elastase after 21 days of culture (scale bar = 20 µm). (E) Size (µm) and colony forming efficiency (CFE %) of organoids obtained from EpCAM^{+} cells from WT or p16$^{-/-}$ mice treated by elastase. (F) Representative images of organoids obtained with EpCAM^{+} from WT and p16$^{-/-}$ without elastase after 21 days of culture (scale bar = 20 µm). (G) Size (µm) and colony forming efficiency (CFE %) of organoids obtained from EpCAM^{+} cells from WT or p16$^{-/-}$ mice. (H) Immunofluorescence of Pro-SpC (red) and KRT8 (green) in WT and p16$^{-/-}$ mice at D21 (scale bar = 20 µm). Quantification of the number of Pre-ADI (Pro-SpC+/KRT8+) among AT2 cells (Pro-SpC+) at D21 (I) and D150 (J) post PBS or elastase treatment in lungs of WT and p16$^{-/-}$ mice. (K) Immunofluorescence of Pro-SpC (white), KRT8 (red) and Krt17 (green) from lungs of emphysematous or control patients (scale bar = 200 µm). (L) Quantification of Pre-ADI (Pro-SpC+/KRT8+) and (M) ADI (Pro-SpC-/KRT8+/KRT17+) among all cells in control and emphysema. (N) UMAP of AT2 cells depending on WT, p16$^{-/-}$ and PBS or elastase treatment at D21 and D150 obtained by FACS sorting and (O) UMAP of AT2 subclustering. (P) Relative frequency of AT2 subpopulations depending on genotypes, treatments and timepoints. (Q) Heatmap of differential expressed genes in WT or p16$^{-/-}$ mice treated by elastase or PBS at D21 and D150. (R) Functional enrichment analysis by time point and pathway category comparing AT2 from WT or p16$^{-/-}$ mice treated by elastase or PBS. *p = 0.05, **p = 0.01, ***p = 0.001, ****p = 0.0001 and ns = not significant

Figure 4: Elimination of senescent cells by senolytics restores epithelial function and reverses emphysema. (A) Experimental design of alveolar organoid formation with EpCAM^{+} cells from WT or p16$^{-/-}$ mice instilled with PBS or elastase cocultured with WT fibroblasts. (B) β-galactosidase activity staining of mouse lungs harvested from p16$^{-/-}$ or WT mice at D21 of elastase instillation (scale bar = 2 mm) and (C) quantification. (D) Representative images of β-galactosidase activity staining on organoids (scale bar = 20 µm) and (E) quantification. (F) Timeline of treatment with senolytics Dasatinib and Quercetin (D+Q) or PEG as control in elastase-treated WT mice. (G) Hematoxylin-eosin staining of the lung at D90 of elastase-treated mice treated with senolytics or PEG as control and (H) quantification of mean linear intercept (MLI). (I) Immunofluorescence staining of Pro-SpC (green) and KRT8 (red). (J) Quantification of the number of AT2 cells among all cells. (K) Quantification of the number of Pre-ADI (Pro-SpC^{+}/KRT8^{+}) cells among AT2 cells. (L) Method of organoids treatment with D+Q or PEG from EpCAM^{+} of WT mouse lungs treated with elastase. (M) Representative images of β-galactosidase activity staining on organoids (scale bar = 20 µm) and (N) quantification of the proportion of senescent organoids. (O) CFE and (P) size of organoids at D14 of culture treated with D+Q or PEG. *p = 0.05, **p = 0.01, ***p = 0.001, ****p = 0.0001 and ns = not significant.

Supplementary

Figure 1: (A) Size (µm) and colony forming efficiency (CFE %) of organoids obtained from the coculture of $EpCAM^+$ cells obtained by magnetic sorting from elastase and PBS treated mice and WT fibroblasts after 14 days of culture. (B) Characteristics of patients from whom AT2 cells were used to generate organoids and clusters. (C) Cluster analysis of the number and size of organoids formed, patient age, smoking history (in pack-years), proportion of emphysema as quantified by chest computed tomography, FEV_1/FVC ratio (%), FEV_1 (%), and TLCO (%) regarding fibroblasts origins. Color intensity reflects the standardized (z-score) value of each variable, allowing visual comparison across patient subgroups. (D) UMAP of 31,172 lung epithelial cell clustering. (E) MatchScore between AT2 subpopulations of our dataset compared with Hu et al. dataset[19]. (F) Activated AT2 signature in available dataset from Conlon et al[17] in mouse exposed to 6 months filter air or cigarette smoke. (G) Activated AT2 signature in AT2 subpopulation in available dataset from Watanabe et al.[18] and in non-smoker, smoker and COPD patients. (H) Activated AT2 signature in AT2 subpopulation in available dataset from Hu et al.[19] and in healthy and COPD patients. FEV_1/FVC ratio (forced expiratory volume in 1 second / forced vital capacity), FEV_1 (forced expiratory volume in 1 second), FVC (forced vital capacity), RV (residual volume) DLCO (diffusion capacity of the lung for carbon monoxide *p = 0.05, **p = 0.01, ***p = 0.001, ****p = 0.0001 and ns = not significant

Figure 2: (A) Functional enrichment analysis by time point and pathway category comparing AT2 from WT mice treated by elastase or PBS at D21, D150 and D21+D150.

Figure 3: (A) Representative images of organoids obtained from the coculture of WT or $p16^{-/-}$ fibroblasts (F-WT and F-$p16^{-/-}$) treated with elastase and WT-$EpCAM^+$ cells also treated with elastase (scale bar = 20 µm) (B) Colony forming efficiency (CFE %) and size (µm) of organoids WT or $p16^{-/-}$ treated with elastase. (C) Cumulative Population doubling level (PDL) of fibroblasts from lungs of WT or $p16^{-/-}$ mice from passage 2 (P2) to passage 7 (P7) (D) Immunohistochemistry of lipofibroblasts by adipose differentiation-related protein (ADRP) staining on lungs of WT and $p16^{-/-}$ mice instilled with PBS or elastase (scale bar = 20 µm). (E) Quantification of the number of lipofibroblasts at D90 post treatment. (F) Quantification of the number of AT2 cells among all cells in WT and $p16^{-/-}$ mice at D21. (G) Dotplot of gene signature of clustered AT2 subpopulations. (H) Partition-based graph abstraction (PAGA) from WT or (I) $p16^{-/-}$ mice treated by elastase depending on AT2 subpopulations and AT1 and corresponding UMAP depending on timepoints.

Figure 4: p16 deletion induces lung regeneration without aberrant process of lung fibrosis

(A) Septal thickness of the alveolar wall, Sirius red area (B) and myofibroblasts (αSMA) quantifications at D21, D90 and D150 in WT or p16$^{-/-}$ mice instilled with PBS or elastase. (D) Lung CT scan analysis of WT and p16$^{-/-}$ mice 12 months after elastase treatment. Relative mRNA quantification of p53 (E) and p21 (F) by RT-qPCR realized 21 days after instillation with PBS or elastase of WT or p16$^{-/-}$ mice. *p = 0.05, **p = 0.01, ***p = 0.001, ****p = 0.0001 and ns = not significant

Figure 1

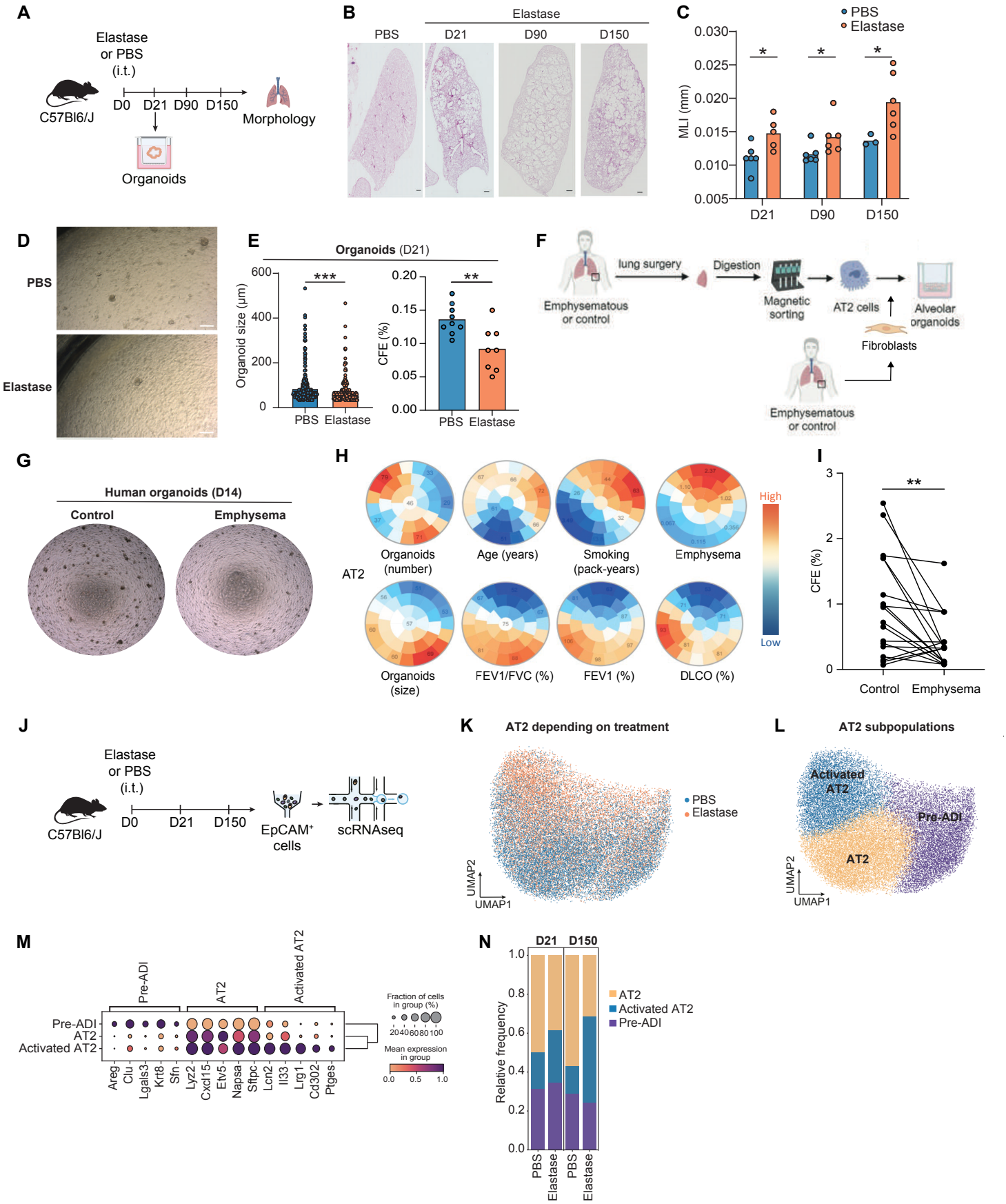
A
Elastase or PBS (i.t.)
C57Bl6/J
D0 D21 D90 D150
Morphology
Organoids
B
Elastase
PBS D21 D90 D150
C
PBS
Elastase
MLI (mm)
D21 D90 D150
D
PBS
Elastase
E
Organoids (D21)
Organoid size (µm)
CFE (%)
PBS Elastase
F
lung surgery
Digestion
Emphysematous or control
Magnetic sorting
AT2 cells
Alveolar organoids
Fibroblasts
Emphysematous or control
G
Human organoids (D14)
Control
Emphysema
H
AT2
Organoids (number)
Age (years)
Smoking (pack-years)
Emphysema
Organoids (size)
FEV1/FVC (%)
FEV1 (%)
DLCO (%)
High
Low
I
CFE (%)
Control Emphysema
J
Elastase or PBS (i.t.)
C57Bl6/J
D0 D21 D150
EpCAM+ cells
scRNAseq
K
AT2 depending on treatment
PBS
Elastase
UMAP2
UMAP1
L
AT2 subpopulations
Activated AT2
Pre-ADI
AT2
UMAP2
UMAP1
M
Pre-ADI
AT2
Activated AT2
Pre-ADI
AT2
Activated AT2
Areg Clu Lgals3 Krt8 Sfn Lyz2 Cxcl15 Etv5 Napsa Sftpc Lcn2 Il33 Lrg1 Cd302 Ptges
Fraction of cells in group (%)
Mean expression in group
N
D21 D150
Relative frequency
AT2
Activated AT2
Pre-ADI
PBS Elastase PBS Elastase

Figure 2

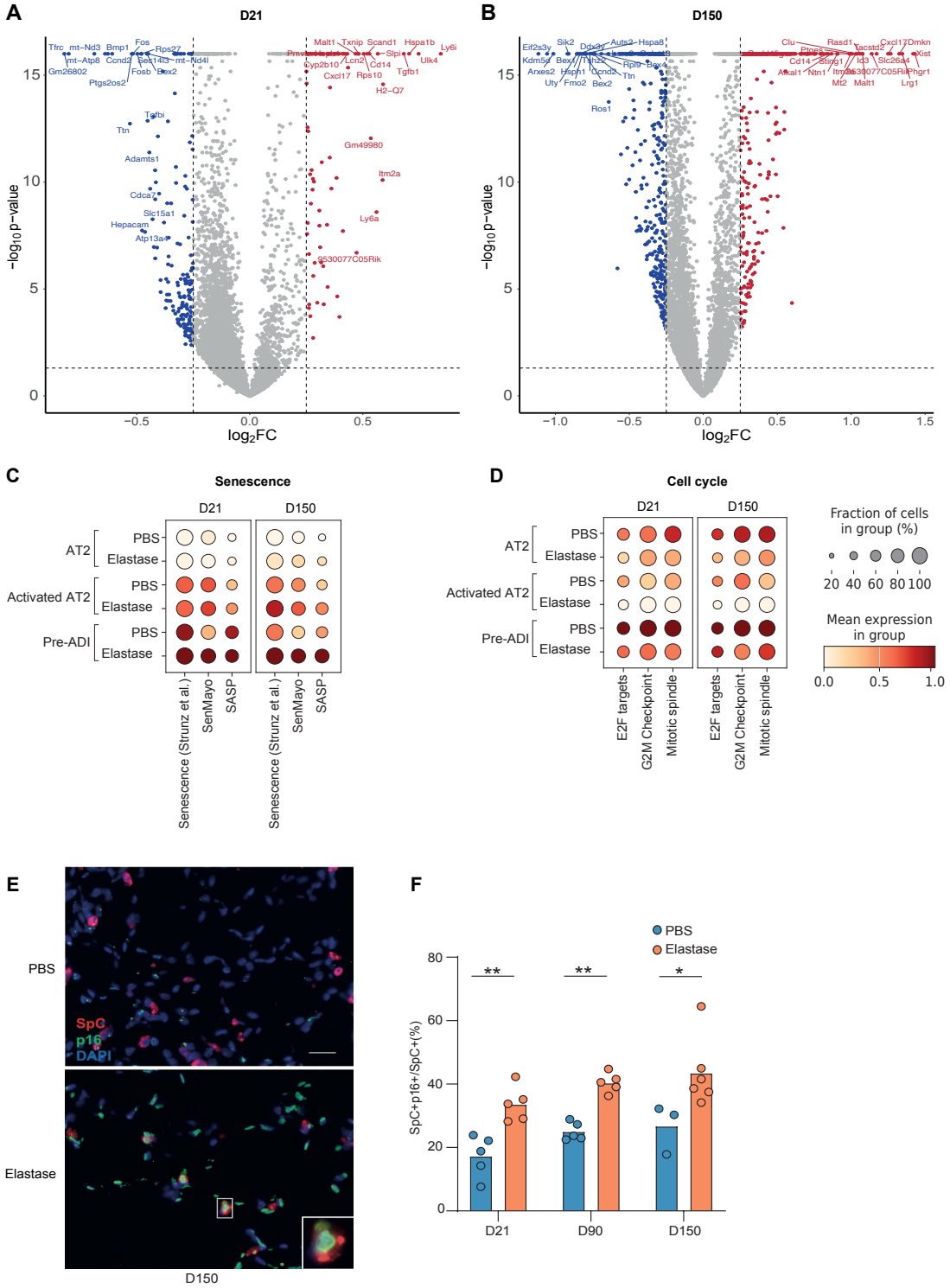
A
D21
B
D150
−log10 p−value
log2FC
C
Senescence
D21
D150
AT2
Activated AT2
Pre-ADI
PBS
Elastase
Senescence (Strunz et al.)
SenMayo
SASP
D
Cell cycle
E2F targets
G2M Checkpoint
Mitotic spindle
Fraction of cells in group (%)
20 40 60 80 100
Mean expression in group
0.0 0.5 1.0
E
PBS
Elastase
SpC
p16
DAPI
D150
F
PBS
Elastase
SpC+p16+/SpC+(%)
D21
D90
D150

Figure 3

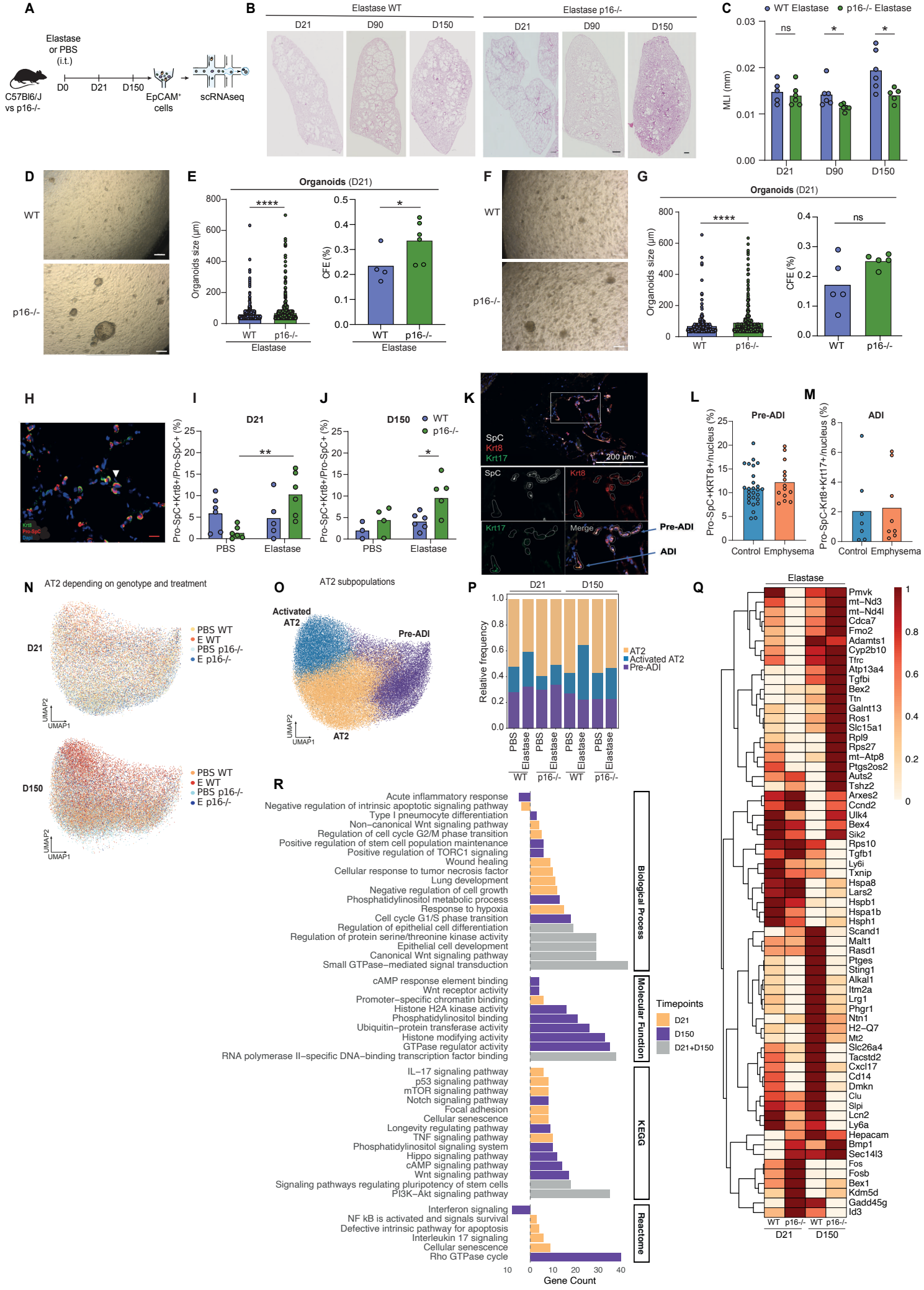
A
Elastase or PBS (i.t.)
C57Bl6/J vs p16-/-
D0
D21
D150
EpCAM+ cells
scRNAseq
B
Elastase WT
Elastase p16-/-
D21
D90
D150
C
WT Elastase
p16-/- Elastase
MLI (mm)
ns
*
*
D21
D90
D150
D
WT
p16-/-
E
Organoids (D21)
Organoids size (µm)
****
CFE (%)
*
WT
p16-/-
Elastase
F
WT
p16-/-
G
Organoids (D21)
Organoids size (µm)
****
CFE (%)
ns
WT
p16-/-
H
Krt8
Pro-SpC
Dapi
I
D21
Pro-SpC+Krt8+/Pro-SpC+ (%)
**
PBS
Elastase
J
D150
WT
p16-/-
Pro-SpC+Krt8+/Pro-SpC+ (%)
*
PBS
Elastase
K
SpC
Krt8
Krt17
200 µm
SpC
Krt8
Krt17
Merge
Pre-ADI
ADI
L
Pre-ADI
Pro-SpC+KRT8+/nucleus (%)
Control
Emphysema
M
ADI
Pro-SpC-Krt8+Krt17+/nucleus (%)
Control
Emphysema
N
AT2 depending on genotype and treatment
D21
PBS WT
E WT
PBS p16-/-
E p16-/-
UMAP2
UMAP1
D150
PBS WT
E WT
PBS p16-/-
E p16-/-
UMAP2
UMAP1
O
AT2 subpopulations
Activated AT2
Pre-ADI
AT2
UMAP2
UMAP1
P
D21
D150
Relative frequency
AT2
Activated AT2
Pre-ADI
PBS
Elastase
WT
p16-/-
Q
Elastase
Pmvk
mt–Nd3
mt–Nd4l
Cdca7
Fmo2
Adamts1
Cyp2b10
Tfrc
Atp13a4
Tgfbi
Bex2
Ttn
Galnt13
Ros1
Slc15a1
Rpl9
Rps27
mt–Atp8
Ptgs2os2
Auts2
Tshz2
Arxes2
Ccnd2
Ulk4
Bex4
Sik2
Rps10
Tgfb1
Ly6i
Txnip
Hspa8
Lars2
Hspb1
Hspa1b
Hsph1
Scand1
Malt1
Rasd1
Ptges
Sting1
Alkal1
Itm2a
Lrg1
Phgr1
Ntn1
H2–Q7
Mt2
Slc26a4
Tacstd2
Cxcl17
Cd14
Dmkn
Clu
Slpi
Lcn2
Ly6a
Hepacam
Bmp1
Sec14l3
Fos
Fosb
Bex1
Kdm5d
Gadd45g
Id3
WT
p16-/-
D21
D150
R
Acute inflammatory response
Negative regulation of intrinsic apoptotic signaling pathway
Type I pneumocyte differentiation
Non–canonical Wnt signaling pathway
Regulation of cell cycle G2/M phase transition
Positive regulation of stem cell population maintenance
Positive regulation of TORC1 signaling
Wound healing
Cellular response to tumor necrosis factor
Lung development
Negative regulation of cell growth
Phosphatidylinositol metabolic process
Response to hypoxia
Cell cycle G1/S phase transition
Regulation of epithelial cell differentiation
Regulation of protein serine/threonine kinase activity
Epithelial cell development
Canonical Wnt signaling pathway
Small GTPase–mediated signal transduction
Biological Process
cAMP response element binding
Wnt receptor activity
Promoter–specific chromatin binding
Histone H2A kinase activity
Phosphatidylinositol binding
Ubiquitin–protein transferase activity
Histone modifying activity
GTPase regulator activity
RNA polymerase II–specific DNA–binding transcription factor binding
Molecular Function
IL–17 signaling pathway
p53 signaling pathway
mTOR signaling pathway
Notch signaling pathway
Focal adhesion
Cellular senescence
Longevity regulating pathway
TNF signaling pathway
Phosphatidylinositol signaling system
Hippo signaling pathway
cAMP signaling pathway
Wnt signaling pathway
Signaling pathways regulating pluripotency of stem cells
PI3K–Akt signaling pathway
KEGG
Interferon signaling
NF kB is activated and signals survival
Defective intrinsic pathway for apoptosis
Interleukin 17 signaling
Cellular senescence
Rho GTPase cycle
Reactome
Gene Count
Timepoints
D21
D150
D21+D150

Figure 4

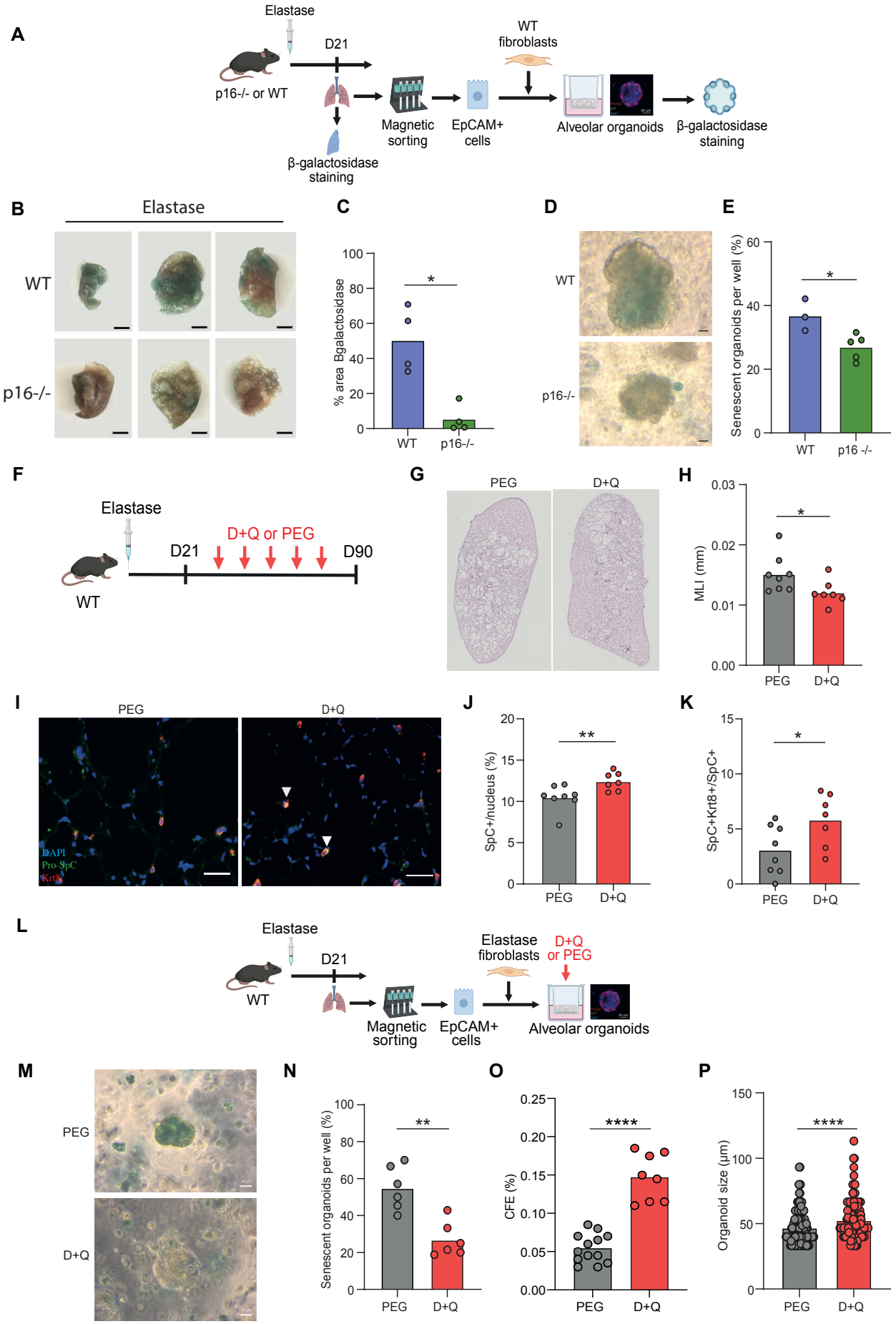
A
Elastase
D21
p16-/- or WT
β-galactosidase staining
Magnetic sorting
EpCAM+ cells
WT fibroblasts
Alveolar organoids
β-galactosidase staining
B
Elastase
WT
p16-/-
C
% area Bgalactosidase
WT
p16-/-
D
WT
p16-/-
E
Senescent organoids per well (%)
WT
p16 -/-
F
Elastase
D21
D+Q or PEG
D90
WT
G
PEG
D+Q
H
MLI (mm)
PEG
D+Q
I
PEG
D+Q
DAPI
Pro-SpC
Krt8
J
SpC+/nucleus (%)
PEG
D+Q
K
SpC+Krt8+/SpC+
PEG
D+Q
L
Elastase
D21
WT
Magnetic sorting
EpCAM+ cells
Elastase fibroblasts
D+Q or PEG
Alveolar organoids
M
PEG
D+Q
N
Senescent organoids per well (%)
PEG
D+Q
O
CFE (%)
PEG
D+Q
P
Organoid size (µm)
PEG
D+Q